International Journal of
Turbomachinery
Propulsion and Power

MDPI

Article

On the Impact of the Off-Design Operating Condition on the Thermal Performance of Rotor Platform Cooling †

Giovanna Barigozzi *, Giovanni Brumana, Nicoletta Franchina and Elisa Ghirardi

Department of Engineering and Applied Sciences, University of Bergamo, 24044 Dalmine, Italy; giovanni.brumana@unibg.it (G.B.); nicoletta.franchina@unibg.it (N.F.); elisa.ghirardi@unibg.it (E.G.)

* Correspondence: giovanna.barigozzi@unibg.it; Tel.: +39-035-2052317

† This manuscript is an extended version of the ETC16-106 paper published in the Proceedings of the 16th European Turbomachinery Conference, Hannover, Germany, 24–28 March 2025.

Abstract

In the present work, off-design operating condition is considered to be the ability of the turbine to operate down to 50% to 20% of its nominal intake air flow rate. An important consequence of these off-design points is the change in the inlet incidence angle, which varied from nominal to −20°. Tests were performed on a seven-blade rotor cascade with platform cooling through an upstream slot simulating the stator-to-rotor interface gap. To model the impact of rotation on purge flow injection, a set of fins were installed inside the slot to give the coolant flow a tangential direction. Different cascades' off-design operating conditions were tested, covering downstream velocity values up to Ma_{2is} = 0.55, with two inlet turbulence intensity levels of 0.6% a and 7%. A thermal measurement campaign was conducted with the Thermochromic Liquid Crystal technique to measure the adiabatic film cooling effectiveness at various coolant-to-main-flow mass flow ratios, different incidence angles, mainstream Mach numbers, and turbulence levels. The results describe the complexity of the turbine operating under off-design operating conditions, relating the improvement in the platform thermal protection to the reduced secondary-flows activity induced by negative incidence.

Keywords: gas turbine; energy transition; rotor cascade; film cooling effectiveness; incidence angle

1. Introduction

Recent trends in power generation focus on minimizing the environmental impact of human activities, driven by growing concerns about the irreversible effects of global warming. Central to the energy transition is the imperative to reduce CO_2 emissions from energy production to mitigate climate change [1]. The competitiveness of renewable energy sources compared to fossil fuels has been rising, particularly in electricity generation. In 2021, renewable primary energy (excluding hydro) increased by approximately 5.1 EJ globally, reflecting an annual growth rate of 15%, up from the previous year's 9% [2]. The share of renewable energy is expected to continue growing in the coming decade. In the short term, gas turbine engines will complement renewables, playing a crucial role in the transition from fossil fuel-based to zero-carbon energy sources. They can help balance energy fluctuations from renewables in the grid and offer immediate emission reductions by utilizing carbon-neutral fuels like ammonia, hydrogen, or bio-jet fuel.

To remain competitive in the market, the new generation of gas turbines must be designed to rapidly ramp up and down, start and shut down quickly, and handle low

Received: 6 June 2025
Revised: 10 December 2025
Accepted: 5 January 2026
Published: 8 January 2026

output levels while adhering to emissions regulations. Fast start-up and shutdown, along with frequent load adjustments to a reduced minimum load, cause engines to operate under more critical thermo-mechanical conditions. This can lead to metal distortions that significantly affect the fluid dynamics of the secondary air system (SAS) and, consequently, the entire engine.

A deeper understanding of aero-thermo-mechanical interactions and more precise predictions of aerodynamics, heat transfer, and cooling flows under variable load conditions are crucial for modern engine designs. Although transient regimes may account for a significant portion of the operational time of industrial gas turbines in future energy production scenarios, knowledge about the behavior of typical SAS components under reduced-minimum-load conditions, and their interactions with the main flow path considering stator/rotor deformations, is currently limited.

Air purged from the later stages of the compressor is directed into the turbine wheel-space at a low radius and exits through the rim seal at the edge of the discs, just before the blade endwall. Labyrinth seals are employed as a contactless solution to minimize leakage between components in relative motion and to regulate the supply of cooling air to the hot-gas path components. Numerous studies document the performance of labyrinth seals, primarily reporting discharge coefficient data [3,4], allowing the derivation of simple 1D-design correlations. The flow through labyrinth seals is highly sensitive to geometric variations caused by changes in rotational speed. Even a 2% change in seal clearance can significantly affect the discharge coefficient [5,6]. To enhance the SAS and overall engine performance, it is crucial to consider off-design flow conditions resulting from large variations in clearance.

The aerodynamic and thermal performance in a gas turbine stage is strongly affected by the interaction between the main and sealing flow, as it emerges from the cavity between the stator and rotor disk. Hot gas ingestion occurs due to a superposition of different mechanisms: (1) externally induced ingress is primarily driven by pressure differences between the high-pressure mainstream flow and the lower pressure in the wheel-space [7]; (2) the rotating rotor blades create a pumping effect that entrains fluid near them, drawing hot gas from the mainstream into the wheel-space [8]. Both mechanisms treat ingress as a result of balancing the radial pressure gradient and the centrifugal forces. Moreover, at reduced injection rates, large-scale, low-frequency pressure fluctuations have been detected in the rim seal flow, whose characteristic wavelength is not connected with the pitch of the blade [9]. These fluctuations can be controlled by conditioning the flow within the cavity in proximity to the rim seal; they disappear increasing the sealing flow [10]. As a result of such preconditioning, the ingress can be suppressed with the additional penalty of the purge flow interacting with secondary flows in the main path [11].

A comprehensive review of the literature on the interaction between the sealing and the main flow is available in [12]. The aerodynamic loss across the rotor increases with the purge flow rate, as demonstrated by Regina et al. [13], due to the strengthening of the horseshoe vortex's pressure-side leg, which traps most of the purged air. As a consequence, the heat load on the first rotor is also increased, which has led designers to use this purge flow not only for sealing but also for cooling purposes. Typically, the sealing of the disk cavity from hot gas ingestion requires a purge-to-mainstream mass flow ratio of the order of 0.7–1.0%. Higher mass fractions may be needed for cooling, as shown by Narzary et al. [14], reporting increased platform cooling effectiveness levels when raising the coolant-to-mainstream mass flow rate (*MFR*). To fully understand the flow and heat transfer phenomena related to the interaction between purge and main flow across the rotor, studies have been conducted on rotating rigs (e.g., [15]) and stationary blade cascades (e.g., Popovic et al. [16]). Few studies have examined the effects of variable

rotational speed [17] and variations in slot dimensions and shapes (e.g., [18,19]). To the best of the authors' knowledge, the impact of mainstream incidence variation has not been previously investigated.

Gas turbine operability depends on load requirements and ambient conditions. Regardless of the cause, in subsonic flow conditions, secondary flows are mitigated while reducing the mass flow at a fixed rotational speed, due to negative incidence to the first rotor blade cascade [20]. However, incidence along the blade span can vary significantly due to the complex flow from the stator, which results from the interaction between swirling combustion gases, coolant flow from the combustor–stator interface gap, and stator secondary flows [11,21,22]. These factors create a highly complex flow pattern that interacts with the sealing flow from the stator–rotor interface gap, affecting its sealing and cooling capabilities. Finally, reducing turbine operability to the minimum load can cause a mismatch between what the compressor delivers to the SAS and what the turbine needs for sealing, potentially compromising the engine's safe operation.

This study is an extended version of a conference paper presented at the 16th European Turbomachinery Conference (ETC16) [23], where the authors complement with film cooling effectiveness data the aerodynamic results obtained by testing a rotor blade cascade with platform cooling under variable incidence conditions [24]. An upstream slot simulates the stator-to-rotor interface gap. Discrete incidence angles from nominal to $-20°$, representing possible off-design flow conditions down to the minimum load, were tested, with the coolant-to-mainstream mass flow rate, *MFR*, varied at a fixed density ratio *DR* = 1.0, inlet turbulence intensity ratio Tu_1 = 7.5%, and Ma_{2is} = 0.4. Selected operating conditions were also tested, reducing the turbulence intensity level down to 0.6% and varying the exit Mach number in the range between 0.2 and 0.55 to provide a wider overview of possible rotor cascade operating conditions at reduced load.

2. Experimental Setup

Tests were conducted using a continuously running, suction-type wind tunnel designed for rotor blade cascades, as illustrated in Figure 1. The wind tunnel's test section contains a 7-blade cascade representative of first-stage, about 0.5 reaction, high-pressure turbines, featuring a pitch-to-chord ratio of 0.637 and an aspect ratio of 1.24 (see Table 1). The cylindrical airfoil profile (Figure 2) mimics the hub section of an industrial first rotor airfoil, and the blade-to-hub junction is crafted with a 3D fillet to replicate the actual engine design.

A slot of 0.042 *C* width, located 0.158 C_{ax} upstream of the leading edge plane, simulates the stator-to-rotor interface gap (Figure 2). Its tangential extension covers three and a half blade passages. In total, 8 fins are installed inside the slot to give the purge flow the proper injection angle of about $-10°$. A plenum supplies the slightly heated compressed air (*DR* about 1.0) to the slot (Figure 3). Please note that the slot assembly shown in Figure 3 is installed upstream of the cascade in the housing shown in Figure 1. The fin's inclination angle is consistent with an engine operating with 1.0% *MFR*. As a general rule, keeping a fixed rotational speed, doubling the *MFR* would roughly result in also doubling the tangential injection angle. In the present investigation the fin's angle was kept constant. Its influence on the cascade's aero-thermal performance was investigated in the past at low speed and will be the object of future investigations. More pieces of information on the facility, the cascade model, and the cooling scheme can be found in [24–26].

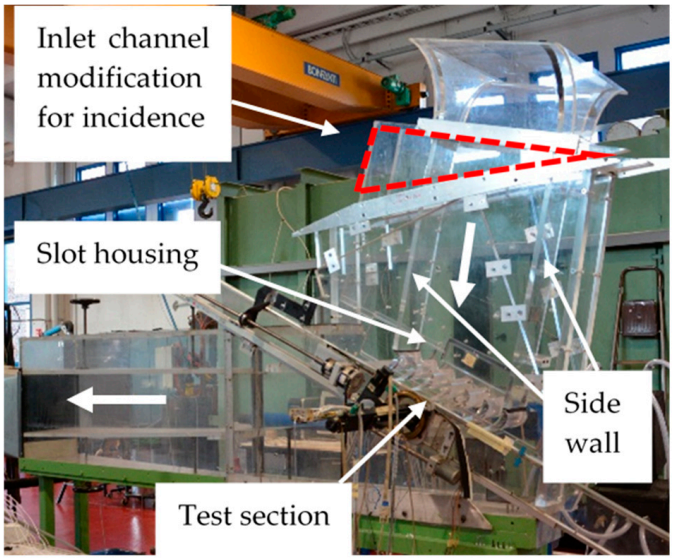

Figure 1. The wind tunnel (the highlighted triangular section and the inclination and length of the side walls are modified to change the direction of the main flow).

Table 1. Cascade geometry and operating conditions.

	Design	Off-Design
$s/C = 0.637$	$Ma_{2is} = 0.55$	$Ma_{2is} = 0.2–0.4$
$H/C = 1.24$	$Tu_1 = 7.5\%$	$Tu_1 = 0.6\%$
$\beta_1 = 30.87°$	$Re_{2is} = 1.51 \times 10^6$	$Re_{2is} = 0.55–1.1 \times 10^6$

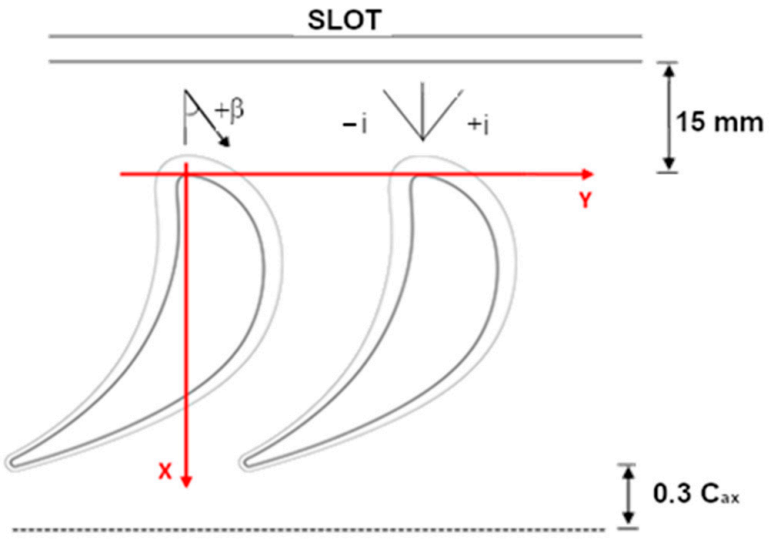

Figure 2. The cascade model.

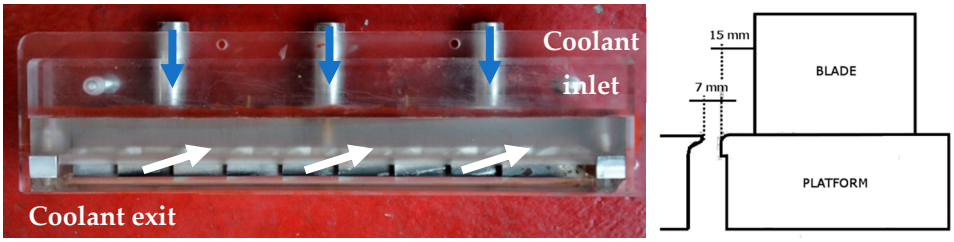

Figure 3. Slot design.

The nominal case prescribes Ma_1 = 0.24, roughly corresponding to a downstream isentropic Mach number of Ma_{2is} = 0.55, and a high inlet turbulence intensity of Tu_1 = 7.5% (see Table 1). Further tests were run at variable mainstream conditions, both in terms of Mach number (Ma_{2is} = 0.2 and 0.4) and turbulence intensity (Tu_1 = 0.6%). The high-turbulence case was obtained by installing a grid formed by cylindrical rods in the wind tunnel inlet section [26]. In all cases, the rotor cascade inlet flow angle was varied from 0° incidence (nominal) down to −20° incidence, with a regular step of 10°. These discrete incidence variations (−20°, −10°, 0°) were obtained by modifying the wind tunnel inlet section design. As an example, Figure 1 shows the setup for the lowest tested incidence case (i = −20°), where a triangular sector is added, and the side wall length and inclination are modified to obtain the prescribed incidence. Finally, coolant injection was varied over a range of *MFR* values up to 2.0%, injecting slightly heated air as coolant. This range is large enough to cover any possible engine operating condition. Table 1 summarizes the test matrix. Please note that changing the *MFR* resulted in small variations in the downstream Mach number. For consistency, tests at variable *MFR* (and constant incidence) were run by fixing the inlet Mach number rather than the outlet Mach number. In this way all share the same mainstream mass flow rate.

3. Measurement Technique

A 3-hole aerodynamic probe located 1.0 C_{ax} upstream of the leading edge plane, a T-type thermocouple, and pressure taps at 0.5 C_{ax} from the trailing edge plane were used to monitor the cascade operating conditions (δMa = ±0.01). An orifice device (δm_c < ±2.1%), pressure taps (δp_c = ±10 Pa), and T-type thermocouples (δT_c = ± 0.5 °C) installed in the supply plenum were used to control the coolant injection conditions. The latter were characterized in terms of coolant-to-mainstream mass flow ratio *MFR*, whose uncertainty was estimated, based on a 95% confidence interval, to always be below δMFR = ±0.1%.

Film cooling effectiveness distributions over the platform surface were obtained using the Wide-Banded Thermochromic Liquid Crystal (TLC) technique [27]:

$$\eta = \frac{T_{aw} - T_\infty}{T_c - T_\infty} \quad (1)$$

TLC is a well-known technique, and it has been widely applied by the authors [28,29]. So only a few details are here recalled. We used 10 °C bandwidth TLCs. To minimize the influence of illumination and viewing angle, they were calibrated in situ by substituting the vane central passage with an instrumented flat aluminum plate (10 calibrated T-type thermocouples, δT = ±0.1 °C), providing the relationship between temperature and the hue parameter shown in Figure 4 and an uncertainty of δT_{aw} = ±0.3 °C. The surface was illuminated by means of two strips of white light LEDs, while a Nikon D7100 camera acquired the color play of the TLCs. A steady test approach was adopted to obtain the adiabatic film cooling effectiveness. RGB to hue conversion was applied to a single image recorded when a stable temperature distribution was established on the surface. This typically happens 30 s to 40 s after injection, avoiding the appearance of significant conduction effects at slot edges. Film cooling effectiveness uncertainty depends on TLC and thermocouple measurements (δT_∞ = ±0.1 °C) and conduction effects. Conduction effects are minimized thanks to the relatively large thickness (35 mm) of the endwall (Plexiglas-made), to the design of the plenum, and to the careful selection of the image to be processed. Based on a 95% confidence interval, the uncertainty in the η value ranges from ±4.2% with η = 0.8, up to about ±15% when η = 0.1.

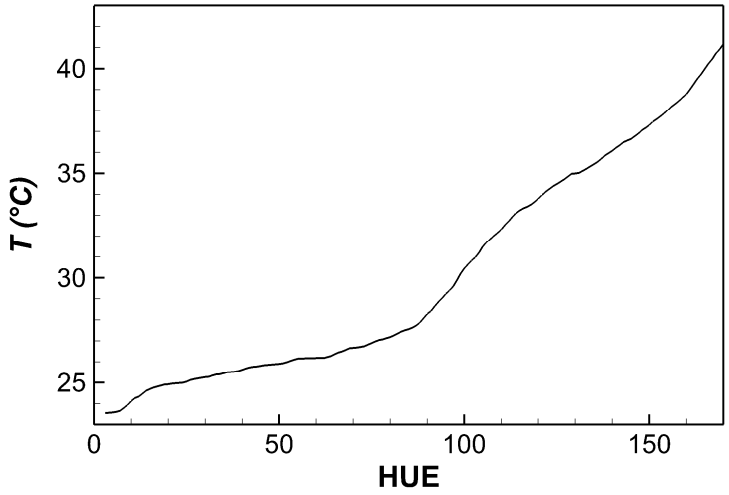

Figure 4. TLC calibration curve.

4. Aerodynamic Background

The cascade aerodynamic behavior of this cooled-rotor blade cascade was assessed by the authors [24], measuring the kinetic energy coefficient ζ downstream of the cascade by means of a miniaturized five-hole probe. The cascade was tested at a nominal operating condition (Ma_{2is} = 0.55 and Tu_1 = 7.5%), variable incidence (i = 0°, −10° and −20°), and variable coolant injection conditions (from uncooled to MFR = 2.0%), with −10° fins inside the slot. Laser Doppler Velocimetry was used to verify the approaching-flow incidence angle and periodicity and injection angle of the coolant. Local loss and vorticity distributions, secondary velocity vectors, pitch, and mass-averaged data supported the discussion of the combined impact of incidence and coolant injection on cascade aerodynamic performance. Figure 5 reports the local kinetic energy loss coefficient at two incidences (i = 0° and −20°) and a fixed MFR = 2.0% on the left and the mass-averaged overall kinetic energy loss coefficient on the right, the latter computed as follows:

$$\bar{\bar{\zeta}} = \frac{\bar{\bar{U}}_{2is}^2 - \bar{\bar{U}}_2^2}{\overline{U}_{2is,ms}^2} \tag{2}$$

According to the literature, a negative incidence was shown to reduce secondary-flows generation and development across the cascade, with a consequent reduction in the endwall cross-flow and in the overall losses. Conversely, losses were significantly increased by raising the coolant flow rate, regardless of the incidence of the cascade. The combination of negative incidence and coolant injection significantly reduced loss production at low incidence (i = −20°) and high MFR. A moderate negative incidence (i = −10°) combined with high MFR values gave rise to a huge loss generation and a significant deterioration of the flow quality approaching the following stator, due to huge variations in the flow angle spanwise distribution. These findings are consistent with the expected underlying flow physics: purge flow injection at a low momentum and with a negative tangential direction enforces the secondary flows, and particularly the horseshoe vortex pressure-side leg. This negative effect can be somewhat counterbalanced by an incidence decrease, which promotes a secondary flows reduction.

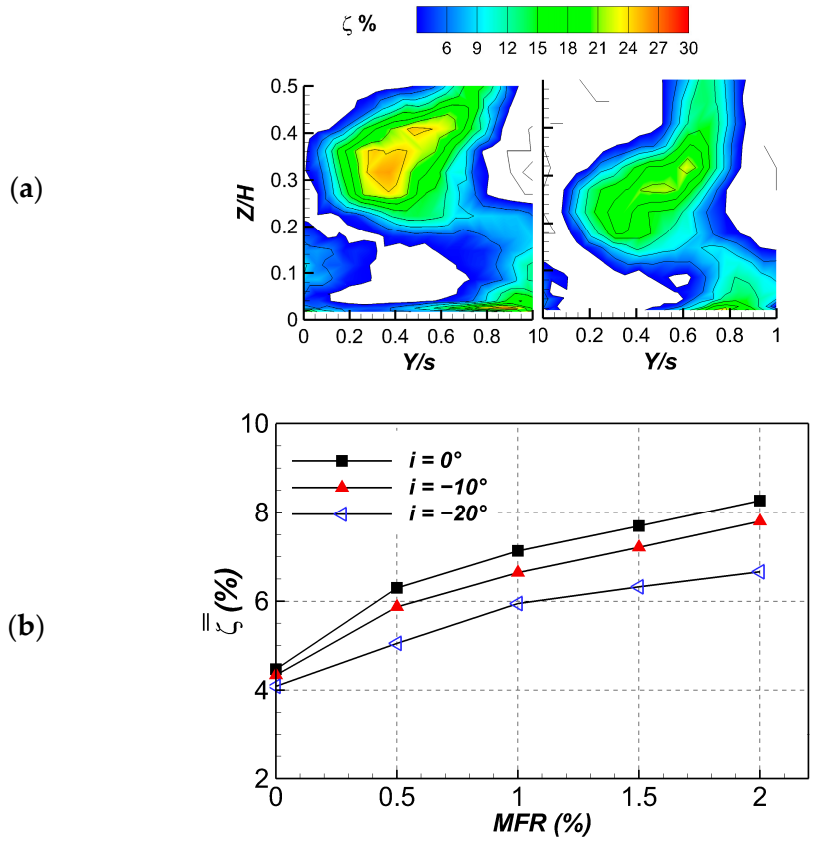

Figure 5. (**a**) Local ζ distributions for $i = 0°$ and $-20°$ ($MFR = 2.0\%$) and (**b**) overall ζ for variable *MFR* and *i* [24].

5. Results

The experimental results provided information regarding the thermal behavior of the considered rotor platform cooling scheme with variable *MFR*, in the range between 0.5% and 2.0%, and variable-inlet flow incidence from nominal down to $-20°$. Before discussing the influence of incidence on film cooling effectiveness distribution, flow visualization results are presented to qualify the impact of incidence variation on secondary-flows evolution and to support the following thermal analysis.

5.1. Flow Visualization

Figure 6 shows the oil and dye flow visualization results obtained by testing the uncooled cascade (i.e., without the slot installed) at $Ma_{2is} = 0.4$ and $Tu_1 = 7.5\%$, varying the incidence. The discontinuity just upstream of the blade leading edge is due to the modular manufacturing of the platform. As expected, traces of separation lines are clearly identified for all tested cases, both on the platform front side (Figure 6—left) and on the blade suction side (Figure 6—right). In agreement with the results coming from the aerodynamic investigation, when progressively reducing the incidence, the stagnation point moves more and more toward the suction side of the blade, according to a blade load reduction. The load decrease, reducing the secondary-flows intensity, results in a translation of the passage vortex separation line toward the trailing edge and in the reduction in the passage vortex extension in the spanwise direction. In this way, the passage vortex impacts the suction side of the adjacent blade further downstream. This is expected to provide better conditions for the thermal protection of the platform at negative incidence.

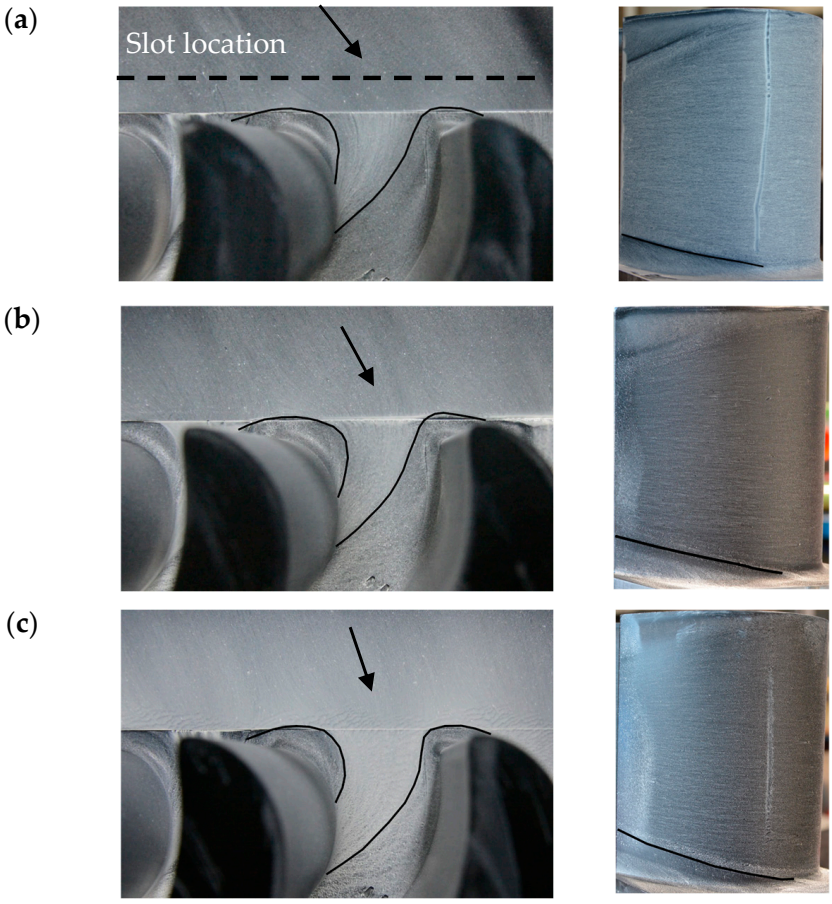

Figure 6. Oil and dye flow visualization at variable i on the platform and on the blade SS: (**a**) 0°, (**b**) −10°, and (**c**) −20° (arrows indicate the inlet flow direction).

5.2. Film Cooling Effectiveness

5.2.1. Influence of i and MFR at Ma_{2is} = 0.4 and Tu_1 = 7.5%

Figure 7 shows the film cooling effectiveness distributions measured at the same cascade operating conditions (Ma_{2is} = 0.4, Tu_1 = 7.5%) for the three tested incidences of 0°, −10°, and −20° and variable coolant injection in the range of MFR from 0.5% to 2.0%. Each contour plot shows the cascade central passage, located at the slot mid-tangential extension. As the presented pictures clearly show, progressively increasing the MFR results in an increased thermal protection, both approaching the blade leading edge and inside of the passage, whatever the incidence. Reducing the incidence at a fixed MFR results in a different coolant footprint at the wall, depending on the injection ratio. When the MFR = 0.5%, coolant is discharged over a wider slot tangential extension when i = −20°, compared to in the other cases. This results in better coverage inside the passage, with the coolant impacting the blade suction side further downstream, thanks to the reduced passage vortex activity. By increasing the MFR, the coolant footprint inside the passage is promoted, reducing i, but coolant is never allowed to cross the passage vortex separation line, limiting the thermal protection to the passage front side.

At a moderate MFR and 0° incidence, the purge flow ejection is not uniform along the slot tangential direction, but it is mostly concentrated on the suction side, leaving the pressure side of the front passage uncooled. This agrees well with the results reported by Green et al. [30], who tested a 0.72% purge mass flow ratio, and with those from Suryanarayanan et al. [31], obtained by testing a full stage at a variable rotational speed. When reducing the incidence, coolant ejection moves towards the pressure side, resulting in increased thermal protection inside the passage. This is consistent with the reduced passage

vortex activity, which reduces the endwall cross-flow, promoting the coolant persistency further downstream inside the channel. At an *MFR* = 1.5%, coolant is discharged almost uniformly along the slot tangential direction, resulting in good thermal protection, even approaching the blade leading edge, especially at −20° incidence. A further increase in the *MFR* up to 2.0% only marginally improves the coolant performance. It is worth mentioning that a two-peak distribution appears when the *MFR* becomes larger than 1.0%. Indeed, a second high-effectiveness region develops approaching the blade pressure side, especially at −20° incidence. This has to be connected to the interaction between the purge flow and the pressure-side leg of the horseshoe vortex, which is attenuated by negative incidence values.

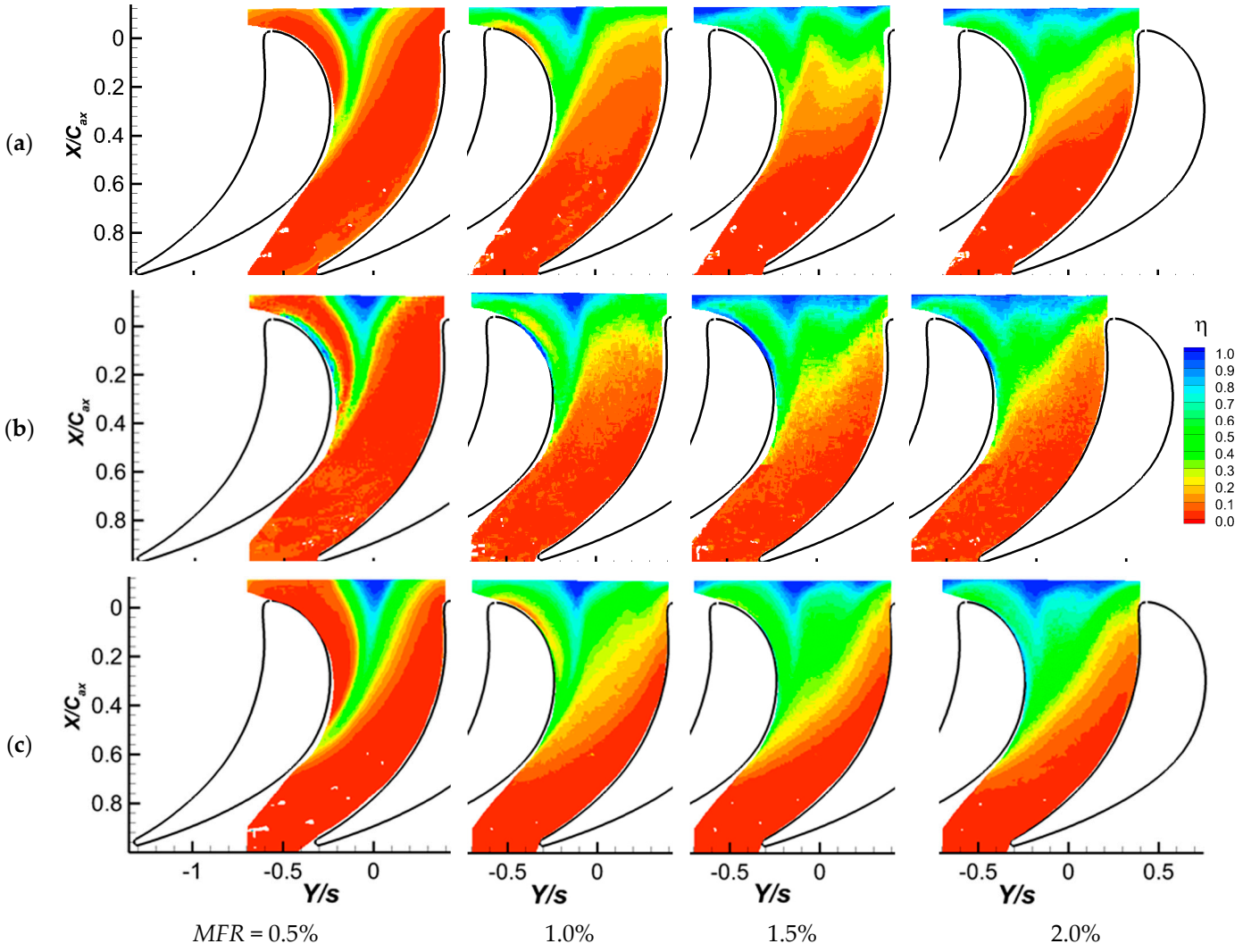

Figure 7. Film cooling effectiveness for variable *MFR* at: (**a**) 0°, (**b**) −10°, and (**c**) −20° incidence.

Based on the flow visualizations of Figure 6, and specifically on the change in position of the corner vortex-related separation line on the blade suction side, we can state that, probably, the coolant will also be able to protect the blade rear-suction-side region below this separation line (this is sometimes called phantom cooling). And since this separation line reduces its radial penetration at negative incidence, we can expect a reduced thermal protection in that region, especially at −20°.

To quantify changes in effectiveness induced by the combined effect of incidence and *MFR* variation, local distributions were averaged along the pitch-wise direction. Figure 8 shows the pitch-averaged effectiveness distributions for the design and the

−20° incidence, with a variable *MFR*, while Figure 9 directly compares the three tested incidence values at a fixed *MFR* = 1.5%. A smooth decrease in effectiveness characterizes all tested conditions, with almost zero value reached between X/C_{ax} = 0.6 and 0.7, depending on incidence and *MFR* values. As previously observed, increasing *MFR* always results in increased η_{av} levels, especially in the channel entrance region. A relevant increase takes place when raising the *MFR* from 0.5% to 1.0%. Further increasing the *MFR*, the gain in effectiveness progressively reduces: it is almost null when $i = 0°$, while at $i = -20°$ it is still detectable. Moreover, for this last case, effectiveness values of the order of 0.1 are still observed up to X/C_{ax} = 0.6, while they are almost null when $i = 0°$. Finally, comparing the different i cases at a constant *MFR* = 1.5% allows us to appreciate the increase in thermal protection due to a strong negative incidence of −20°. Conversely, a limited incidence reduction of −10° does not give significant improvement in the platform thermal protection.

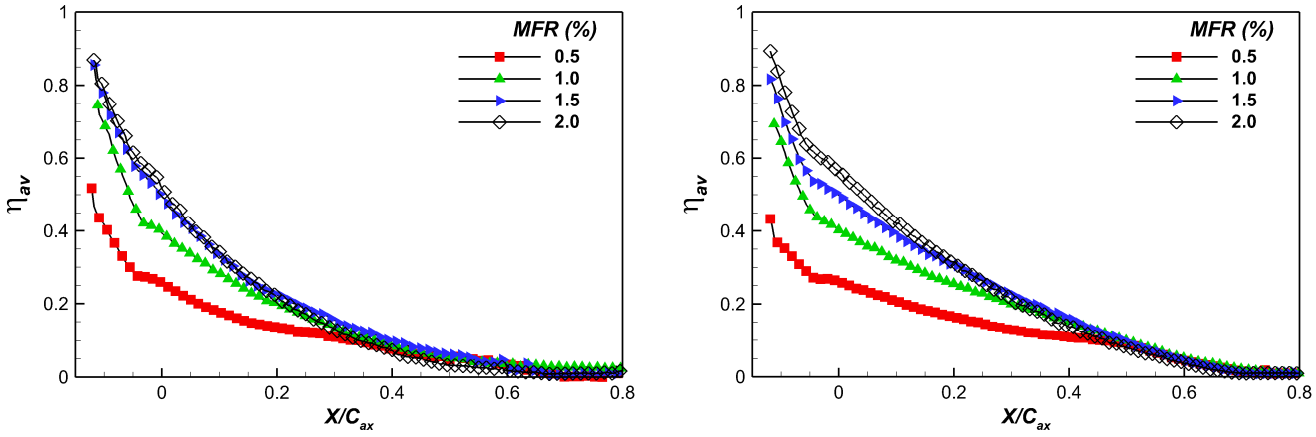

Figure 8. Pitch-averaged η for variable *MFR* at: (**a**) 0° and (**b**) −20° incidence.

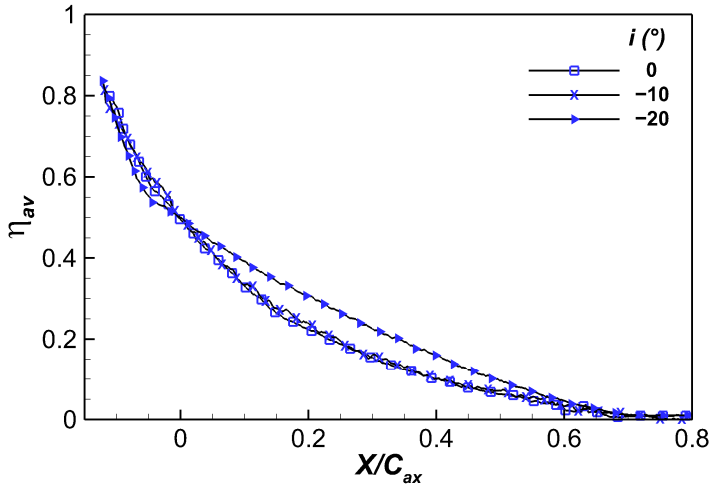

Figure 9. Pitch-averaged η at *MFR* = 1.5% and variable *i*.

Finally, area-averaged film cooling effectiveness values were also computed, averaging in the axial direction from slot exit to $0.8C_{ax}$. Figure 10 shows that a significant change in the incidence of −20° is responsible for an increase in the area-averaged effectiveness of about 0.03 when *MFR* is larger than 0.5. This gain reduces to 0.008 when the incidence reaches −10°.

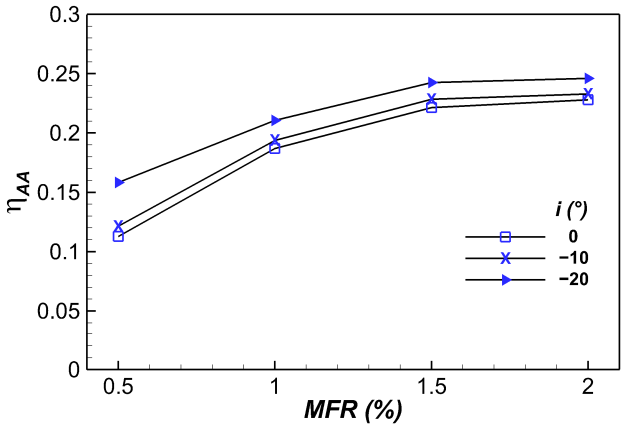

Figure 10. Area-averaged η for variable *MFR* and *i* (Ma_{2is} = 0.4 and Tu_1 = 7.5%).

5.2.2. Influence of Ma_{2is} and Tu_1

Similar data were also collected by reducing the downstream Mach number to 0.2 and increasing its level up to 0.55, the cascade nominal operating condition. Moreover, a set of tests was performed at Ma_{2is} = 0.4 without the turbulence generator, resulting in a reduced Tu_1 = 0.6%. For the sake of space, Figure 11 shows the results corresponding to an *MFR* of 1.5% and variable Mach at 0° and −20° incidence, while Figure 12 shows similar data obtained at the reduced Tu_1 level. These data should be compared with those reported in Figure 7.

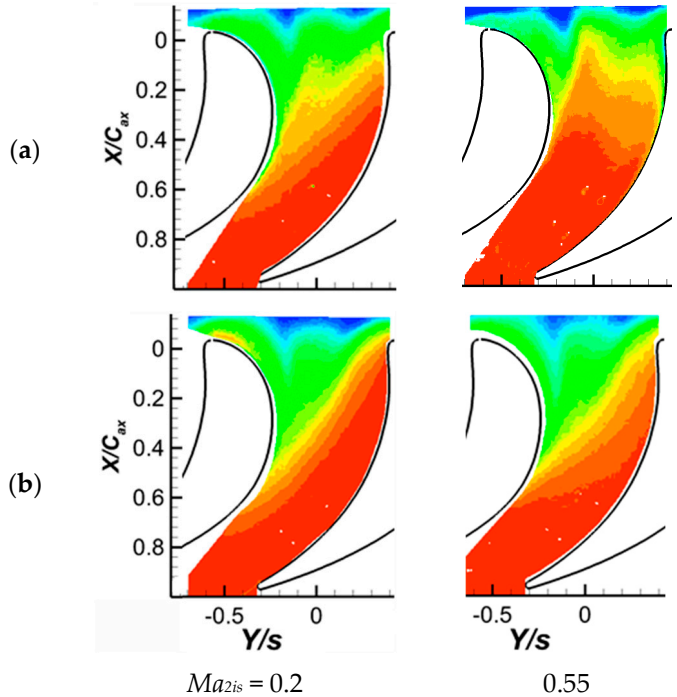

Figure 11. η distributions for variable Ma_{2is} and *MFR* = 1.5% at: (**a**) 0°, and (**b**) −20° incidence.

First, considering the impact of freestream velocity (Figure 11), only small differences can be observed in the local film cooling effectiveness distributions measured at the two incidence conditions. In particular, a different coolant footprint takes place on the platform front side when increasing the exit Mach number to 0.55 at 0° incidence. This could be related to the concentration of passage vortex activity at the wall, resulting in a stronger cross-flow. Reducing *i* down to −20°, a very similar effectiveness distribution is observed for the different tested Ma_{2is} values, with only a slight reduction in the thermal protection

inside the passage when Ma_{2is} reaches 0.2, as a consequence of the increased intensity of secondary flows. Finally, reducing the freestream turbulence intensity level (Figure 12) results in a reduction in thermal protection, especially in the leading edge region, where turbulence promotes the coolant distribution at the wall.

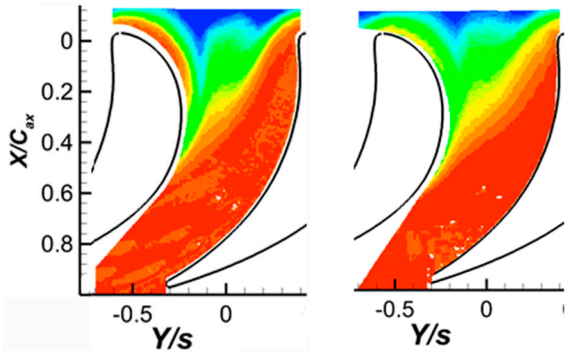

(**a**) (**b**)

Figure 12. η distributions (Tu_1 = 0.6%, Ma_{2is} = 0.4 and MFR = 1.5%): (**a**) 0°, and (**b**) −20° incidence.

To quantify the impact of Ma_{2is} and Tu_1 on thermal protection, pitch-averaged values were again computed for all tested conditions, and the resulting distributions are reported in Figure 13. These data highlight the different behavior of slot platform cooling when changing the freestream conditions. In particular, at i = 0°, all tested Ma_{2is} values show almost the same decreasing trend, besides the local differences previously observed. Small variations are instead observed at i = −20°, with a slight progressive increase in performance raising Ma_{2is}. These small variations are consistent with the limited change in the inlet Mach number (from 0.11 to 0.24).

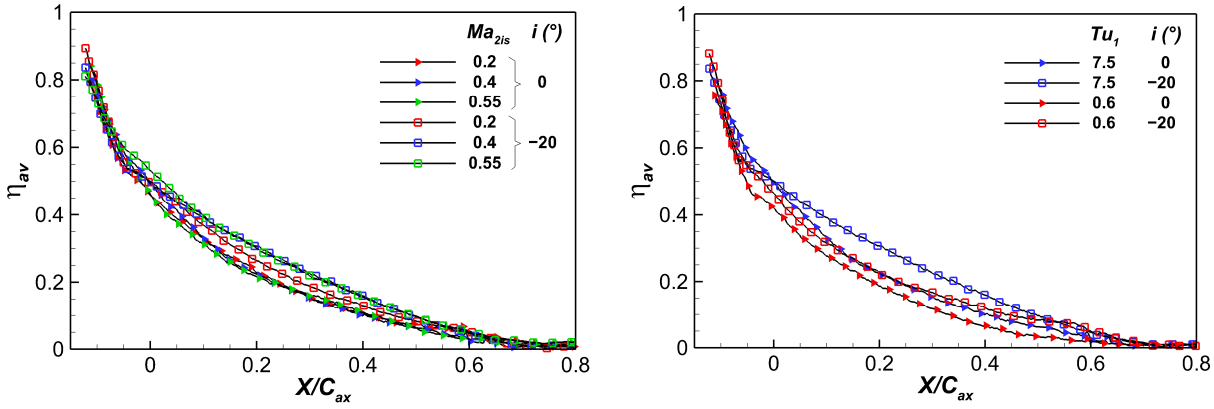

(**a**) (**b**)

Figure 13. Pitch averaged η (MFR = 1.5%) at variable: (**a**) Ma_{2is} and i and (**b**) Tu_1 and i.

Turbulence intensity (Figure 13b) appears to play a more significant role in determining the thermal performance of platform cooling through the slot. A high turbulence intensity promotes the coolant presence at the wall, resulting in a general rise in the pitch-averaged distribution, whatever the approaching flow direction.

Finally, to sum up the results from the previous discussion, area-averaged values were also computed and reported in Figure 14. Again, only data related to the 0° and −20° incidence cases are reported, since those obtained at −10° are very similar to the 0° case. The reported curves show that neither the Mach number's nor the turbulence

intensity's influence on film cooling effectiveness changes when reducing the incidence, when taking the whole-platform point of view.

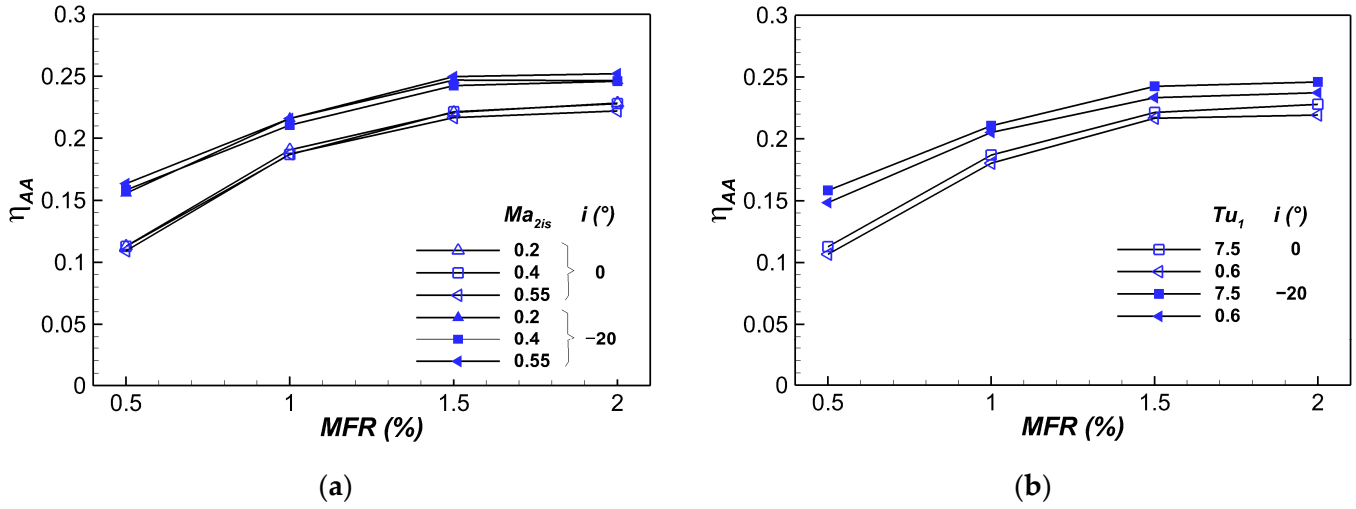

Figure 14. Area-averaged η at variable: (**a**) Ma_{2is} and i and (**b**) Tu_1 and i (Ma_{2is} = 0.4).

More specifically, a change in the freestream Mach number has a negligible impact on the overall performance, while reducing the turbulence intensity slightly reduces the thermal protection, whatever the coolant injection condition. As an example, at $i = 0°$ an average reduction of 0.007 is observed in the area-averaged effectiveness, which becomes -0.008 when the incidence is reduced to $-20°$.

6. Conclusions

Thermal measurements were carried out in a rotor cascade under realistic engine conditions to evaluate the performance of a platform cooling scheme simulating the stator-to-rotor interface gap at various *MFR* values between 0.5% and 2.0% with main flow incidence angles of 0°, $-10°$, and $-20°$. A sensitivity analysis to changes in mainstream flow condition, in terms of Mach number and turbulence intensity level, was also carried out. The objective was to evaluate the thermal performance of this cooled-blade cascade by simulating some effects of low-load operating conditions. These data complement the aerodynamic results obtained by testing the same cascade model at similar operating conditions [25]. The key highlights of the present study are the following:

- As expected, since negative incidence reduces secondary-flows generation and development across the cascade, improved film cooling effectiveness distributions are observed at negative incidence, especially at $-20°$. An incidence reduction of $-10°$ instead only marginally impacts the thermal protection. In all cases, coolant only protects the passage front portion, as it is not allowed to cross the passage vortex-related 3D separation line.
- In the investigated *MFR* range, increasing the coolant flow rate always results in a better thermal protection of the front platform region, whatever the incidence. It is worth noting that the gain in effectiveness decreases when increasing *MFR*.
- When considering both thermal and aerodynamic aspects, a compromise has to be found since aerodynamic losses increase with rising *MFR*. A good solution is found at an *MFR* of 1.5%: at design condition ($i = 0°$), the overall loss increases by $\Delta\zeta = +3.22\%$, with the area-averaged film cooling effectiveness reaching $\eta_{AA} = 0.22$. At reduced incidence ($i = -20°$), the extra loss due to film cooling decreases to $\Delta\zeta = 2.23\%$, while η_{AA} increases up to 0.25.

- A change in mainstream flow condition (Ma_{2is} and Tu_1) marginally modifies the platform thermal protection. In addition to some local differences in the film cooling effectiveness distribution, both pitch-averaged and area-averaged data almost coincide when changing the free-stream Mach number, while a decrease in the approaching turbulence intensity level results in a slight decrease in thermal protection. At $MFR = 1.5\%$ and design incidence, a $\Delta\eta_{AA} = -0.005$ is observed, almost doubling at $-20°$ incidence.

Finally, the results of this experimental thermal investigation, together with those related to the aerodynamic behavior, provide data to support the design process of a stator-to-rotor interface gap for flexible gas turbine operation.

Author Contributions: Conceptualization, G.B. (Giovanna Barigozzi); methodology, G.B. (Giovanna Barigozzi) and N.F.; investigation, G.B. (Giovanni Brumana) and E.G.; data curation, G.B. (Giovanna Barigozzi); writing—original draft preparation, G.B. (Giovanna Barigozzi), G.B. (Giovanni Brumana), N.F. and E.G.; writing—review and editing, G.B. (Giovanna Barigozzi) and N.F.; visualization, G.B. (Giovanni Brumana) and E.G.; supervision, G.B. (Giovanna Barigozzi). All authors have read and agreed to the published version of the manuscript.

Funding: This research received no external funding.

Data Availability Statement: The original contributions presented in this study are included in the article. Further inquiries can be directed to the corresponding author.

Acknowledgments: The authors would like to thank Raffaele Cainero for his contribution to the experimental activity.

Conflicts of Interest: The authors declare no conflicts of interest.

List of Symbols

The following abbreviations are used in this manuscript:

C	blade chord
$DR = \rho_c/\rho_\infty$	density ratio
H	blade height
i	flow incidence angle
$Ma = U/a$	Mach number
$MFR = m_c/m_\infty$	mass flow rate (%)
P	Pressure
$Re_{2,is} = U_{2is}C/\nu$	isentropic outlet Reynolds number
s	blade pitch
T	temperature
$Tu = u'/U$	turbulence Intensity (%)
u, v, w	velocity components
U	mean velocity
X, Y, Z	cascade coordinate system
W	slot width
β	flow angle
ν	kinematic viscosity
η	film cooling effectiveness
ζ	kinetic energy loss coefficient
Superscript	
‘	RMS
-	pitch-averaged
=	area- or mass-averaged

Subscript	
ax	Axial
aw	adiabatic wall
c	Coolant
is	isentropic condition
1	rotor inlet
2	rotor exit
∞	Mainstream

References

1. Ray, A.; De, S. Renewable Electricity Generation–Effect on GHG Emission. In *Encyclopedia of Renewable and Sustainable Materials*; Hashmi, S., Choudhury, I.A., Eds.; Elsevier: Amsterdam, The Netherlands, 2020; pp. 728–735.
2. BP Statistical Review of World Energy 2022, 71st Edition. Available online: https://www.bp.com/content/dam/bp/business-sites/en/global/corporate/pdfs/energy-economics/statistical-review/bp-stats-review-2022-full-report.pdf (accessed on 17 July 2024).
3. Bozzi, L.; D'Angelo, E.; Facchini, B.; Micio, M.; Da Soghe, R. Experimental Investigation on Leakage Losses and Heat Transfer in a Non-Conventional Labyrinth Seal. In Proceedings of the ASME Turbo Expo 2011: Turbine Technical Conference and Exposition, Vancouver, BC, Canada, 6–10 June 2011; Paper No. GT2011-46362.
4. Szyma'nski, A.; Wroblewski, W.; Bochon, K.; Majkut, M.; Strozik, M.; Marugi, K. Experimental validation of optimised straight-through labyrinth seals with various land structures. *Int. J. Heat Mass Transf.* **2020**, *158*, 119930. [CrossRef]
5. Nayak, K.C. Effect of Rotation on Leakage and Windage Heating in Labyrinth Seals with Honeycomb Lands. *J. Eng. Gas Turbines Power* **2020**, *142*, 081001. [CrossRef]
6. Fraczek, D.; Bochon, K.; Wroblewski, W. Influence of Honeycomb Land Geometry on Seal Performance. In Proceedings of the ASME Turbo Expo 2016: Turbomachinery Technical Conference and Exposition, Seoul, Republic of Korea, 13–17 June 2016; Paper No. GT2016-57569.
7. De Cosmo, G.; Scobie, J.A.; Lock, G.D.; Sangan, C.M.; Carnevale, M. Fluid Dynamics of Turbine Rim Seal Structures: A Physical Interpretation Using URANS. *J. Eng. Gas Turbines Power* **2023**, *145*, 031009. [CrossRef]
8. Graikos, D.; Tang, H.; Carnevale, M.; Bailey, N.Y.; Scobie, J.A. Rotationally induced ingress in rotor–stator systems. *Phys. Fluids* **2024**, *36*, 075141. [CrossRef]
9. Vella, S.; Tang, H.; Carnevale, M.; Scobie, J.A.; Lock, G.D.; Salvatori, F.; Sangan, C.M. On the relationship between swirl and unsteadiness within turbine rim seals. *J. Eng. Gas Turbines Power* **2025**, *147*, 041031. [CrossRef]
10. Darby, P.W.; Mesny, A.W.; De Cosmo, G.; Carnevale, M.; Lock, G.D.; Scobie, J.A.; Sangan, C.M. Conditioning of leakage flows in gas turbine rotor–stator cavities. *J. Eng. Gas Turbines Power* **2021**, *143*, 021009. [CrossRef]
11. Schreiner, B.D.J.; Wilson, M.; Li, Y.S.; Sangan, C.M. Effect of Purge on the Secondary Flow-Field of a Gas Turbine Blade-Row. *J. Turbomach.* **2020**, *142*, 101006. [CrossRef]
12. Barigozzi, G.; Abdeh, H.; Rouina, S.; Franchina, N. The Aero-Thermal Performance of Purge Flow and Discrete Holes Film Cooling of Rotor Blade Platform in Modern High Pressure Gas Turbines: A Review. *Int. J. Turbomach. Propuls. Power* **2022**, *7*, 22. [CrossRef]
13. Regina, K.; Kalfas, A.I. Experimental investigation of purge flow effects on a high pressure turbine stage. *J. Turbomach.* **2015**, *135*, 041006. [CrossRef]
14. Narzary, D.P.; Liu, K.C.; Rallabandi, A.P.; Han, J.C. Influence of coolant density on turbine blade film-cooling using pressure sensitive paint technique. *J. Turbomach.* **2012**, *134*, 031006. [CrossRef]
15. Schuepbach, R.S.; Abhari, M.G.; Rose, T.; Germain, I.; Raab, J.G. Effects of Suction and Injection Purge-Flow on the Secondary Flow Structures of a High-Work Turbine. *J. Turbomach.* **2010**, *132*, 021021. [CrossRef]
16. Popovíc, I.; Hodson, H.P. Aerothermal impact of the interaction between hub leakage and mainstream flows in highly-loaded high pressure turbine blades. *J. Turbomach.* **2013**, *135*, 061014. [CrossRef]
17. Suryanarayanan, A.; Mhetras, S.P.; Schobeiri, M.T.; Han, J.C. Film-Cooling Effectiveness on a Rotating Turbine Platform using Pressure Sensitive Paint Technique. *J. Turbomach.* **2010**, *132*, 041001. [CrossRef]
18. Lynch, S.P.; Thole, K.A. Heat Transfer and film cooling on a contoured blade endwall with platform gap leakage. *J. Turbomach.* **2017**, *139*, 051002. [CrossRef]
19. Barigozzi, G.; Franchini, G.; Perdichizzi, A.; Maritano, M.; Abram, R. Purge flow and interface gap geometry influence on the aero-thermal performance of a rotor blade cascade. *Int. J. Heat Fluid Flow* **2013**, *44*, 563–575. [CrossRef]
20. Perdichizzi, A. Mach Number Effects on Secondary Flow Development Downstream of a Turbine Cascade. *J. Turbomach.* **1990**, *112*, 643–651. [CrossRef]

21. Abdeh, H.; Barigozzi, G.; Perdichizzi, A.; Henze, M.; Krueckels, J. Incidence Effect on the Aero-Thermal Performance of a Film Cooled Nozzle Vane Cascade. *J. Turbomach.* **2019**, *141*, 051005. [CrossRef]
22. Chen, A.F.; Shiau, C.C.; Han, J.C. Turbine blade platform film cooling with simulated swirl purge flow and slashface leakage conditions. *J. Turbomach.* **2017**, *139*, 031012. [CrossRef]
23. Barigozzi, G.; Brumana, G.; Franchina, N.; Ghirardi, E. On the impact of Off-Design Condition on the Thermal Per-formance of Rotor Plat-form Cooling. In Proceedings of the 16th European Turbomachinery Conference, Hannover, Germany, 24–28 March 2025. Available online: https://www.euroturbo.eu/29092025/publications/proceedings-papers/etc2025-106/ (accessed on 11 December 2025).
24. Abdeh, H.; Barigozzi, G.; Franchina, N. Rotor Cascade Assessment at Off-Design Condition: An Aerodynamic Investigation on Platform Cooling. *Int. J. Turbomach. Propuls. Power* **2023**, *8*, 23. [CrossRef]
25. Barigozzi, G.; Franchini, G.; Perdichizzi, A.; Maritano, M.; Abram, R. Influence of purge flow injection angle on the aerothermal performance of a rotor blade cascade. *J. Turbomach.* **2014**, *136*, 041012. [CrossRef]
26. Barigozzi, G.; Perdichizzi, A.; Pestelli, L.; Abram, R. Combined Experimental and Numerical Investigation of the Aero-Thermal Performance of a Rotor Blade Cascade with Platform Cooling. In Proceedings of the ASME Turbo Expo 2019: Turbomachinery Technical Conference and Exposition, Phoenix, AZ, USA, 17–21 June 2019; Paper No. GT2019-91601.
27. Camci, C.; Kim, K.; Hippensteele, S.A. A New Hue Capturing Technique for the Quantitative Interpretation of Liquid Crystal Images Used in Convective Heat Transfer Studies. *J. Turbomach.* **1992**, *114*, 765–775. [CrossRef]
28. Barigozzi, G.; Perdichizzi, A.; Henze, M.; Krueckels, J. Aerodynamic and Heat Transfer Characterization of a Nozzle Vane Cascade with and without Platform Cooling. In Proceedings of the ASME Turbo Expo, Montreal, QB, Canada, 15–19 June 2015; Paper No. GT2015-42845. [CrossRef]
29. Barigozzi, G.; Benzoni, G.; Franchini, G.; Perdichizzi, A. Fan-shaped Hole Effects on the Aero-Thermal Performance of a Film Cooled Endwall. *J. Turbomach* **2006**, *128*, 43–52. [CrossRef]
30. Green, B.R.; Mathison, R.M.; Dunn, M.G. Time-averaged and Time-accurate Aerodynamic Effects of Rotor Purge Flow for a Modern, One and One-half Stage High-pressure Turbine-Part II: Analytical Flow Field Analysis. *J. Turbomach* **2012**, *136*, 011009. [CrossRef]
31. Suryanarayanan, A.; Mhetras, S.P.; Schobeiri, M.T.; Han, J.C. Film cooling effectiveness on a rotating blade platform. *J. Turbomach.* **2009**, *131*, 011014. [CrossRef]